International Journal of Pressure Vessels and Piping 217 (2025) 105557

Contents lists available at ScienceDirect

International Journal of Pressure Vessels and Piping

journal homepage: www.elsevier.com/locate/ijpvp

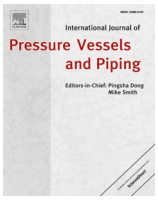

A study on annealing temperature in FEM simulation of residual stress in SUS316 weld

Lina Yu [a,*], Kenji Suzuki [b], Hiroyuki Hirata [a], Kazutoshi Nishimoto [a], Kazuyoshi Saida [a]

[a] The University of Osaka, 2-1 Yamadaoka, Suita, Osaka, 565-0871, Japan
[b] Niigata University, 8050 Ikarashi 2-no-cho, Nishi-ku, Niigata, 950-2181, Japan

ARTICLE INFO

Keywords:
Austenitic stainless steel
Annealing temperature
Recrystallization
FEM
Residual stress

ABSTRACT

This study investigates the recrystallization phenomenon of strain hardening during welding process in austenitic stainless steel (SUS316), and a suitable annealing temperature for finite element method (FEM) simulation was proposed. The electron backscatter diffraction (EBSD) analysis results of a 1-pass weld with prior surface machining proved that the annealing effect can be introduced owing to the recrystallization phenomenon caused by welding thermal cycle. Therefore, it was necessary to introduce a suitable annealing temperature into the FEM simulation to simulate this phenomenon. To establish a propriate annealing temperature, the 20 % and 30 % pre-strained cold-rolled specimens were subjected to peak temperatures ranging from 800 °C to 1300 °C, held at the peak temperature for 1 s, and their corresponding hardness was measured. The results showed that when the annealing temperature is approximately 1050 °C, the resulting hardness aligns with that of solution-treated specimens. To verify the accuracy of the proposed annealing temperature in the FEM simulation, this determined annealing temperature (1050 °C) was then applied in the FEM model to estimate the residual stress after 7-layer welding, with the results validated through measurements. The good agreement between the simulated residual stress and the measured results follows that the proposed annealing temperature of 1050 °C in FEM simulation is reasonable and effective. Therefore, the annealing temperature of 1050 °C should be included in the FEM simulation of SUS316 welding in the future.

1. Introduction

Stress corrosion cracking (SCC) is a major problem common in welded components of austenitic stainless steel used in nuclear power plants. SCC is caused by the combined effects of three factors: material, environment, and stress. Among these, high tensile residual stress is an important factor that results in the SCC of materials [1,2]. Austenitic stainless steels, such as SUS316, tend to work hardening due to their FCC crystal structure and low stacking fault energy. During multi-layer welding, high plastic strain can accumulate in austenitic stainless steel [3]. However, the accumulated strain hardening can be reduced or even eliminated during welding thermal cycles due to recrystallization, recovery [4,5], and grain growth below the melting point, which is called the annealing effect [6]. The influence of the annealing effect must be investigated to accurately predict the residual stresses induced by welding in the joints of austenitic stainless steels. It should be noted that the concept of "annealing" in this study is different from the concept of "annealing" in heat treatment process. In this study, it is only used to describe the recrystallization phenomenon of strain hardening during welding process.

Thermo-elastic-plastic finite element method (FEM), a method of obtaining residual stress that is as important as experimental measurement, has been widely used to predict residual stress in welds [7–9]. Ignoring the annealing effect will significantly affect the formation of accumulated plastic strain and welding residual stress, resulting in a significant overestimation of the FEM simulation results [10–12]. Therefore, establishing a reasonable annealing model in FEM simulation has important theoretical significance and practical engineering value for high-precision prediction of residual stress in austenitic stainless steel welding.

Early studies on the numerical simulation of welding generally did not consider the influence of the annealing effect, therefore, tended to use plastic models with a constant yield surface size (such as the ideal elastic-plastic model and moving hardening models) for finite element analysis [10–12]. In the past 20 years, some researchers have used the isotropic hardening models and mixed hardening models in FEM

* Corresponding author.
E-mail address: yulina@mapse.eng.osaka-u.ac.jp (L. Yu).

https://doi.org/10.1016/j.ijpvp.2025.105557
Received 28 December 2024; Received in revised form 28 April 2025; Accepted 16 May 2025
Available online 17 May 2025

simulations to consider the strain hardening of materials and have developed a variety of annealing models to consider the annealing softening phenomenon during welding [13–19]. However, the proposed annealing models still have some problems. For example, the dynamic annealing model based on the equivalent annealing parameters divides the annealing process into two stages according to the equivalent annealing parameters; however, its control equation has the problem of discontinuity [17]. Some dynamic annealing models consider the effects of annealing temperature, time, and initial hardening degree. However, the models are relatively complex and difficult to use widely [18,19].

Among the proposed annealing models, the single-stage annealing model has been widely used because of its simplicity. In the simulation model, it is typically assumed that the accumulated strain hardening is eliminated when the material reaches a preset temperature (i.e., the annealing temperature). Various researchers have proposed different annealing temperatures for austenitic stainless steels. Deng et al. suggested that the annealing temperature of SUS316 steel should be in the range of 800–1000 °C [6,20,21]. Ihara et al. used a melting temperature of 1400 °C as the annealing temperature for SUS316L steel [22]. In 2021, Li et al. suggested that the annealing temperature of austenitic stainless steels should be 1000 °C [23]. In summary, the single-stage annealing model concludes that the recommended annealing temperature of SUS316 austenitic stainless steel is approximately in the range of 800–1400 °C. The recommended annealing temperature range for SUS316 steel is significantly large, which confuses subsequent researchers conducting FEM simulations of multilayer welding in SUS316 steel.

Especially for the actual welding process of SUS316 pipes, butt welding is performed after surface machining, which is conducted to match the inner diameter of pipes and smooth the surface finish [22]. Moreover, both the surface machining and the subsequent welding processes generate residual stress. Due to the thermal effect of the subsequent welding process, the initial residual stress distribution generated by surface machining would be released by the recrystallization phenomenon (annealing effect) at temperatures above the annealing temperature. This means that the initial residual stress distribution would vary depending on the subsequent welding thermal cycles. Therefore, when surface machining is performed before welding, determining the appropriate annealing temperature in FEM simulation is more important for predicting the welding residual stress of SUS316 austenitic stainless steel with high accuracy. Thus, a reasonable annealing temperature for SUS316 steel in the FEM simulation is investigated in detail in this study.

The outline of this manuscript's overall structure is as follows. First, in order to confirm whether the annealing effect due to welding thermal cycle occurs, the recrystallization phenomenon near the fusion zone of a 1-pass weld with prior surface machining was investigated through EBSD analysis. Then, to establish a suitable annealing temperature, the 20 % and 30 % pre-strained cold-rolled specimens were subjected to peak temperatures ranging from 800 °C to 1300 °C, held at the peak temperature for 1 s, and their corresponding hardness was measured. Based on the results of hardness, the appropriate annealing temperature was obtained. Finally, to verify the accuracy of the proposed annealing temperature for SUS316 steel in FEM simulation, the determined annealing temperature was then applied in the FEM model to estimate the residual stress after 7-layer welding, and the simulated results were verified with the experimentally measured results.

2. Materials and methods

2.1. Materials

SUS316 steel, which is an austenitic stainless steel, was chosen as the base material for this study. YS316 was used as the welding wire, which exhibits a chemical composition similar to that of the base metal. Their chemical compositions are given in Table 1.

2.2. Thermal heat treatment

To simulate the welding-induced strain, 20 % and 30 % pre-strained specimens were prepared. To improve uniformity and prevent temperature rise during cold-rolling process, the plate materials were cold-rolled by multiple passes at low speed and low reduction rate, with final strains of 20 % and 30 %. The test pieces were cut from the central part of the cold-rolled sample using electrical discharge machining, which would cause the minimal damage to the original state of the material.

In order to study the effect of recrystallization caused by the welding thermal cycle on strain hardening during welding, the pre-strained cold-rolled specimens were heated to different peak temperatures with a holding time of 1 s to simulate the welding thermal cycle during welding. Thermal heat treatment was conducted using a high-frequency heating device. The heating rate was 100 °C/s, and the peak temperature changed at 800–1300 °C (800, 900, 1000, 1050, 1100, 1200 and 1300 °C) for 1 s, followed by cooling in an atmosphere of pure argon with the cooling rate of approximately 50 °C/s. In addition, for comparison, some specimens were annealed at 1100 °C for 1 h and then quenched in water for solution treatment (ST).

2.3. Vickers hardness measurement

Vickers hardness tests were performed to examine the changes in hardness after the thermal heat treatment. After polishing, the hardness of the sample was measured under a load of 0.098 N for 15 s. The maximum and minimum values were excluded from 14 measurements and the average hardness value was taken.

2.4. Microstructure observation methods

Microstructure observation was carried out using the scanning electron microscopy (SEM) and the electron backscatter diffraction (EBSD). Before SEM observation, the specimens were polished and electrolytically etched using the 10 % oxalic acid solution. Before EBSD analysis, the specimens were electrolytically polished using the 15 % perchloric acid ethanol at 5.0 V and 0.5 A for approximately 30 s.

To investigate the changes in strain and crystal orientation near the sample surface processed by surface machining, EBSD was used for crystal orientation analysis. The IQ (Image Quality) map shows the signal strength of the EBSD pattern. Areas where the pattern is unclear, that is, where the crystal orientation is disturbed by lattice deformation, tend to appear darker. Therefore, it is possible to estimate the presence of local deformation. The IPF (Inverse Pole Figure) map illustrates the crystal orientation of the grains. Fig. 1 shows the schematic of the KAM (Kernel Average Misorientation) map, which represents the crystal orientation misorientation between adjacent pixels. The KAM value is the average value of the crystal orientation misorientation of six points near each measurement point, corresponding to the plastic strain

Table 1
Chemical composition of the used materials (mass %).

Material	C	Si	Mn	P	S	Ni	Cr	Mo	Co	Fe
SUS316	0.04	0.60	0.93	0.034	0.004	10.16	16.83	2.06	0.20	Bal.
YS316	≦0.08	≦0.65	1.0–2.5	≦0.03	≦0.03	11.0–14.0	18.0–20.0	2.0–3.0	–	Bal.

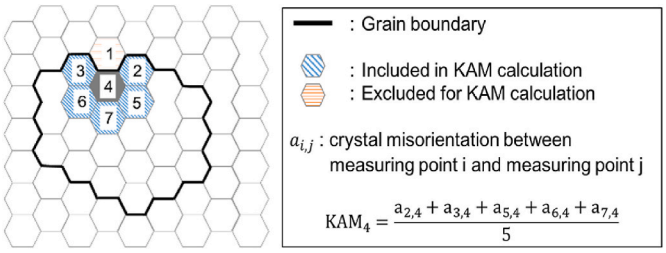

Fig. 1. Schematic of kernel average misorientation (KAM).

distribution. Fig. 2 shows the schematic of the GOS (Grain Orientation Spread) map, which represents the local misorientation, which is the average misorientation within the same grain. The GOS value is one of the misorientation parameters that is the average misorientation between an arbitrary point and other points within the same grain, and is an index of the magnitude of strain. Fig. 3 illustrates a conceptual diagram of the GROD (Grain Reference Orientation Deviation) map, which shows the orientation difference at each location relative to a reference orientation within the same crystal. The GROD value is a crystal orientation parameter that represents the reference orientation determined for each crystal grain and the orientation difference at each measurement point.

2.5. Welding conditions

Tungsten inert gas (TIG) welding of SUS316 was performed using the YS316 welding wire, exhibiting a chemical composition similar to SUS316. The schematic of the welding specimen is illustrated in Fig. 4, and a U-shaped groove was applied at the center of specimen.

Before welding, the bottom surface of each specimen was machined. The surface machining conditions were set to be close to those of the actual condition, with a cutting speed of 45 m/min, a feed rate of 0.1 mm/rev, and a cutting depth of 0.1 mm. The microstructure of the bottom surface of the sample after surface machining before welding was observed using SEM. An EBSD crystal orientation analysis was also performed to investigate the strain distribution near the machined surface.

To study the effect of recrystallization phenomenon caused by welding thermal cycle on the machined surface, a 1-pass welding was prepared on the specimen shown in Fig. 4, with the welding condition listed in Table 2. After 1-pass welding, the cross section of the weld near the bottom surface was observed by EBSD to investigate the change of the strain distribution.

To verify the reasonable annealing temperature, a 7 layer - 13 pass welding was performed on the specimen shown in Fig. 4, with the welding conditions listed in Table 3. After 7-layer welding, a 40 mm × 14 mm × 5 mm specimen was cut from the center of the welded sample using electric discharge machining (EDM) for residual stress measurement. It should be noted that the stress in the direction perpendicular to the welding direction (σ_x) and the plate thickness direction (σ_z) can be measured by DEM, while the residual stress in the welded direction (σ_y) of the welded specimen was released when it was cut by EDM.

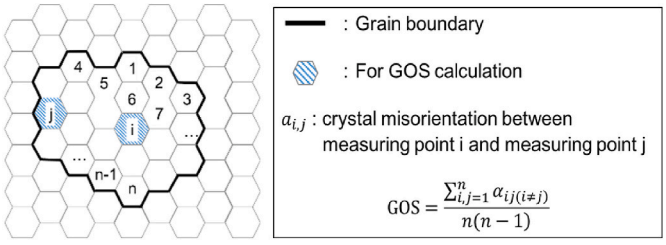

Fig. 2. Schematic of grain orientation spread (GOS).

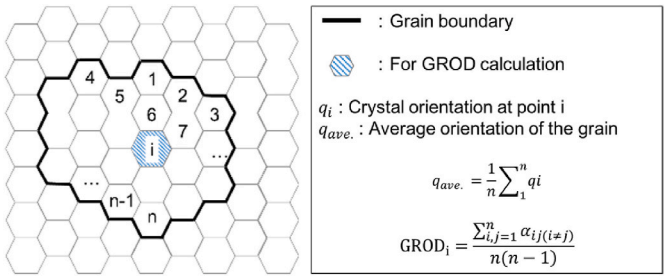

Fig. 3. Schematic of grain reference orientation deviation (GROD).

2.6. Residual stress measurement

The residual stress on the cross section of the 7-layer welded specimen was experimentally measured using the double exposure method (DEM), which was proposed by Suzuki et al. [24]. It has been confirmed that DEM makes it possible to measure the residual stresses of coarse-grained materials and welded parts with white X-rays by combining a CdTe pixel detector capable of energy discrimination in the high-energy region [25].

The synchrotron radiation experiment was carried out using beamline BL19B2 of SPring-8 (Super Photon Ring 8 GeV), a large synchrotron radiation facility at the Japan Synchrotron Radiation Research Center. The X-ray energy was set as 70 keV, the incident beam size was 0.4 × 0.4 mm, and the diffraction plane used for the residual stress measurement was γ-Fe 311 diffraction.

Fig. 5 shows the X-ray beam and detector configurations of the DEM. In the DEM, the distance "L" between detector positions P1 and P2 was set to 400 mm. The diffraction radii at P1 and P2 were *r1* and *r2*, respectively. A CdTe pixel detector was used as an X-ray detector, with the detection area of 201 × 191 pixels and the pixel size of 0.2 × 0.2 mm. An automatic stage was attached to the 2θ arm of the diffractometer, and the detector was mounted on it to measure the diffraction at the front (P1) and back (P2) positions.

As shown in Fig. 5, the measured position was set on the center line of the weld ($x = 0$ mm), and the diffraction in the horizontal direction (x-direction strain) and vertical direction (z-direction strain) was measured at intervals of 0.5 mm within the range of $x = -15 \sim 15$ mm. The coordinate system related to the strain and stress calculations is shown in Fig. 5.

3. Results and discussion

3.1. Annealing effect caused by welding thermal cycle

Fig. 6 shows the microstructure of the bottom surface of the sample after prior surface machining before welding, as observed using SEM. Some fine grains were visible near the machined surface, which are much finer than that of the base metal. To investigate the strain distribution near the machined surface, as shown in the yellow frame in Fig. 6, an EBSD crystal orientation analysis was carried out on the cross section of the specimen. Fig. 7 shows the EBSD maps near the machined surfaces in the yellow frame in Fig. 6. The area under each map represents the machined surface of the specimen. In all KAM, GOS, and GROD maps, the values near the machined surface are higher, clearly indicating that the plastic strain is larger. It follows that the prior surface machining introduced some strain near the bottom surface of the sample.

To investigate the influence of the annealing effect caused by the welding thermal cycle, the microstructure of the bottom surface of the sample subjected to surface machining was observed after 1-pass welding. The microstructure near the fusion line in the cross section after 1-pass welding is shown in Fig. 8. Coarse grains were present in the welded metal (WM), and the grain size in the heat-affected zone (HAZ)

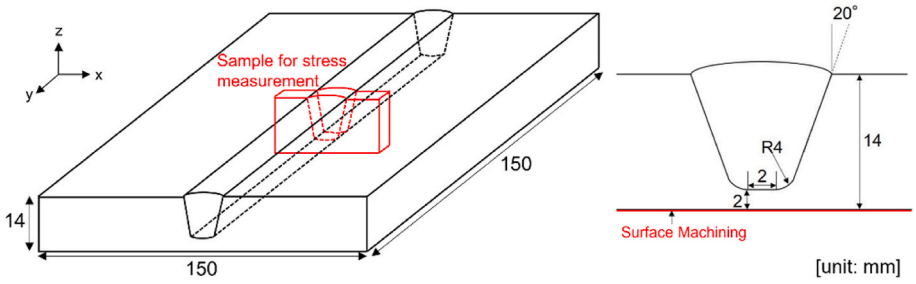

(a) Overall view (b) Groove shape

Fig. 4. Schematic of welding specimen and sample for stress measurement.

Table 2
Welding condition of 1-pass welding.

Pass	Current (A)	Voltage (V)	Wire feed rate (mm/s)	Welding speed (mm/s)
1	250	15–16	45	1.67

Table 3
Welding conditions of 7 layer - 13 pass welding.

Pass	Current (A)	Voltage (V)	Wire feed rate (mm/s)	Welding speed (mm/s)
1	250	15–16	45	1.67
2~13	220	14–15	45	1.67

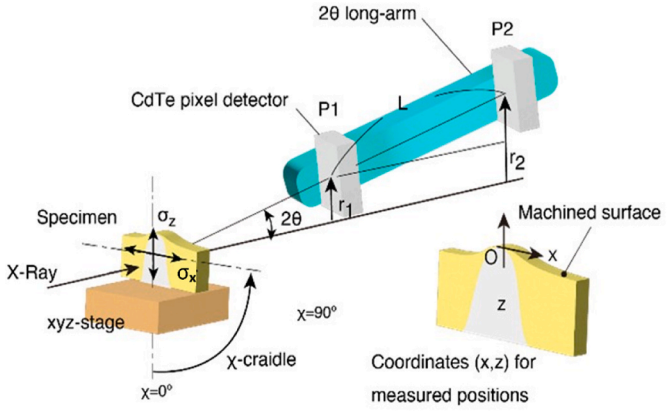

Fig. 5. X-Ray beam and configuration of detector for DEM.

varied according to the distance from the fusion line. There was an evident coarse-grained zone near the fusion line, followed by a fine-grained zone far from the fusion line.

The machined surface near the fusion line (x = 0–2 mm), marked with the yellow frames in Fig. 8, was analyzed using EBSD, and the KAM, GOS, and GROD maps are illustrated in Fig. 9. The EBSD analysis results for the area in the range of $x = 0$, 1, 2 mm from the fusion line are shown in Fig. 9 (a), (b), and (c), respectively. After 1-pass welding, the distribution of the KAM, GOS, and GROD maps shows that the KAM, GOS, and GROD values near the bottom surface are almost the same as those away from the bottom surface, indicating that no significant strain was observed near the machined surface, even in an area 2 mm far from the fusion line. This indicates that the strain introduced by prior surface machining was eliminated because recrystallization or recovery occurred owing to the heat generated by the welding thermal cycle. Therefore, the EBSD analysis results shown in Fig. 9 indicate that annealing can be introduced during welding. The concept of "annealing"

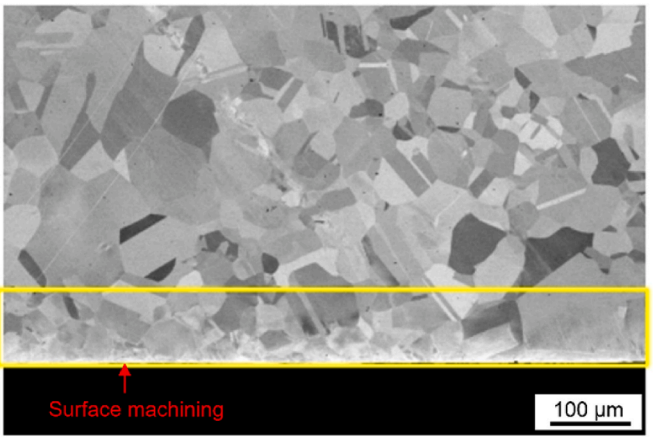

Fig. 6. Microstructure of the bottom surface of the sample with surface machining.

used in this study differs from that used in the heat treatment process. In this study, it was used only to describe the recrystallization phenomenon of strain hardening during welding.

3.2. Investigation of the appropriate annealing temperature of SUS316

In the FEM simulation, the annealing effect exhibited a significant influence on the formation of accumulated plastic strain and welding residual stresses. Ignoring this would lead to a considerable overestimation of the simulation results. Therefore, an appropriate annealing temperature should be confirmed before the FEM simulation of the SUS316 steel.

Hardness is known to be correlated with plastic strain [5]. Therefore, the appropriate annealing temperature was determined based on the change in hardness. In order to explore the effect of recrystallization and recovery caused by welding thermal cycle on the change in hardness, the cold-rolled specimens with 20 % and 30 % pre-strain were heated to different peak temperatures and kept at the temperature for 1 s to simulate the thermal cycle during welding. Vickers hardness was measured after heat treatment, and the results are shown in Fig. 10. The dotted lines represent the hardness value before thermal aging and after solution treatment (ST). It can be observed that the hardness of the 20 % and 30 % cold-rolled specimens both decreased with the increase in peak temperature; when the peak temperature was higher than 1050 °C, even after thermal aging heat treatment for only 1 s, the hardness softened to the same level as ST.

To clarify the relationship between the hardness change owing to thermal aging and the microstructure, the microstructures of 20 % cold-rolled specimens after heat treatment were observed under the same conditions. Fig. 11 shows the microstructures before and after heat treatment. Before heat treatment, the slip lines were observed after 20 %

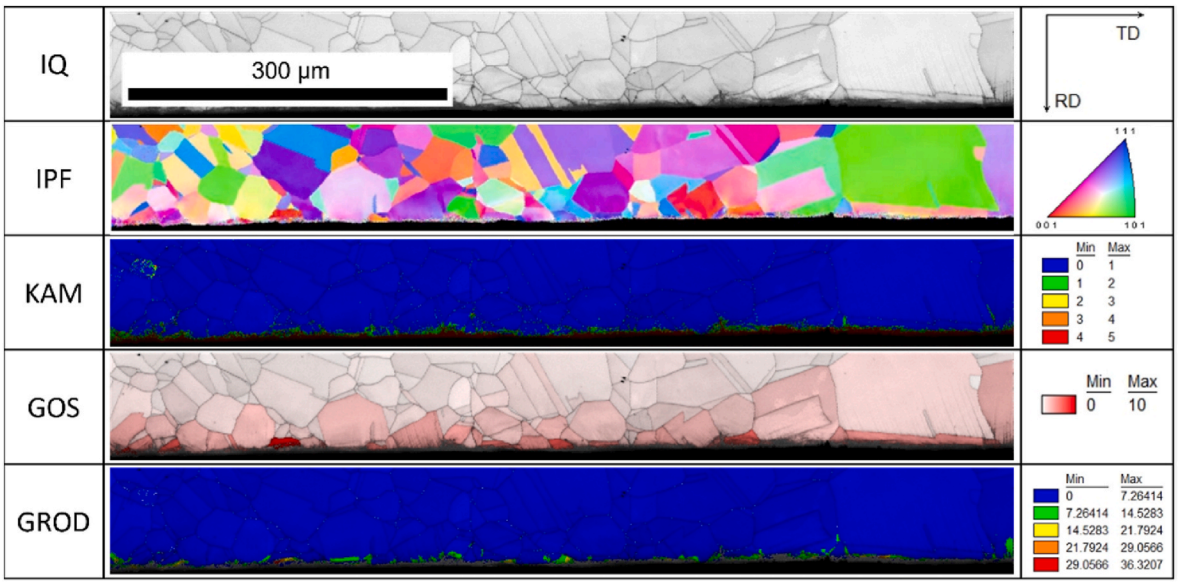

Fig. 7. Crystal orientation maps near the processed surface.

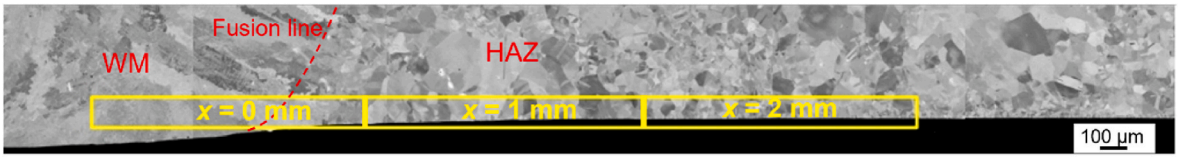

Fig. 8. Microstructure near the fusion line of 1-pass weld with surface machining.

cold rolling. After thermal aging at conditions of 800 °C and 900 °C, the slip lines were still observed, and no significant changes in the microstructure were observed. While after thermal aging at 1000 °C, a small amount of fine grains were found and the slip lines observed after cold-rolling have disappeared, indicating that the recrystallization phenomenon has just started to occur. However, many fine recrystallized grains were observed at 1050 °C even after thermal aging for only 1 s, indicating that recrystallization phenomenon has completely occurred. When the peak temperature was above 1050 °C, the grain size obviously increased with the increase in peak temperature, indicating that the grain growth has occurred at temperatures above 1050 °C. Therefore, softening occurred owing to recrystallization including in areas that were work-hardened by welding, which is why the hardness was reduced to the same level as that of ST.

These results suggest that the work-hardened areas caused by welding can be softened owing to recrystallization and recovery during the welding thermal cycle (annealing effect), and can be softened to ST when the peak temperature of the welding thermal cycle is above 1050 °C due to recrystallization. Therefore, in FEM simulation, the residual stress and plastic strain should be set to zero when the peak temperature of the welding thermal cycle is above 1050 °C, which is the appropriate annealing temperature for SUS316 steel.

3.3. Verification of the accuracy of the proposed annealing temperature

In this study, the accuracy of the proposed annealing temperature of 1050 °C for SUS316 steel in FEM simulation was verified by comparing the simulated residual stress with the experimentally measured results of a 7-layer welded sample.

The residual stress after 7-layer welding were simulated using a sequentially coupled thermo-mechanical FEM software JWRIAN, which is specifically designed to predict the residual stress, thermal history, and deformation of welds [7–9,26]. First, the transient thermal analysis was performed based on the same heat input conditions as the actual welding conditions. Then, the obtained temperature result was used as the thermal load in the subsequent mechanical analysis. In the FEM simulation, the isotropic strain hardening model was employed, and in the strain hardening model, the annealing effect was considered using a single-stage annealing model. The residual stress and plastic strain were set to zero when the peak temperature of the welding thermal cycle was above 1050 °C, which is the proposed annealing temperature for SUS316 steel.

The cross section of the 7-layer weld is illustrated in Fig. 12, and the dotted lines indicate the weld boundary. Based on the actual cross section (Fig. 12) and the actual sample size (Fig. 4), a 3D mesh model of 7-layer weld was created using PATRAN software. The analysis model along with the dimensions and boundary condition is illustrated in Fig. 13. In order to balance the computing time and the calculation accuracy, finer meshes were designed in the WM and HAZ, while relatively coarser grids were arranged in the BM range far away from the WM. The sequence and arrangement of 13 passes welds in the model are shown in Fig. 13 (b), and they are identical to those of experimental mock-up. Near the undersurface of the sample, fine elements were used to simulate the residual stress distribution introduced by surface machining, with the size of the minimum element was 0.1 mm in the depth direction. Four-node generalized plane strain element was used in the analysis. In the thermal analysis, the volumetric heat source with a double ellipsoidal distribution was used to simulate the thermo-mechanical behavior. In the thermal analysis, the peak temperature of weld pool was controlled at the range of 1600–1800 °C. The inter-pass temperature was assumed to be lower than 100 °C during the multi-pass welding process. In addition to the heat source model, both the thermal radiation and the heat convection were considered in the thermal analysis. The boundary condition was a three-point constraint to prevent the rigid body deformation.

According to the actual machining conditions and the

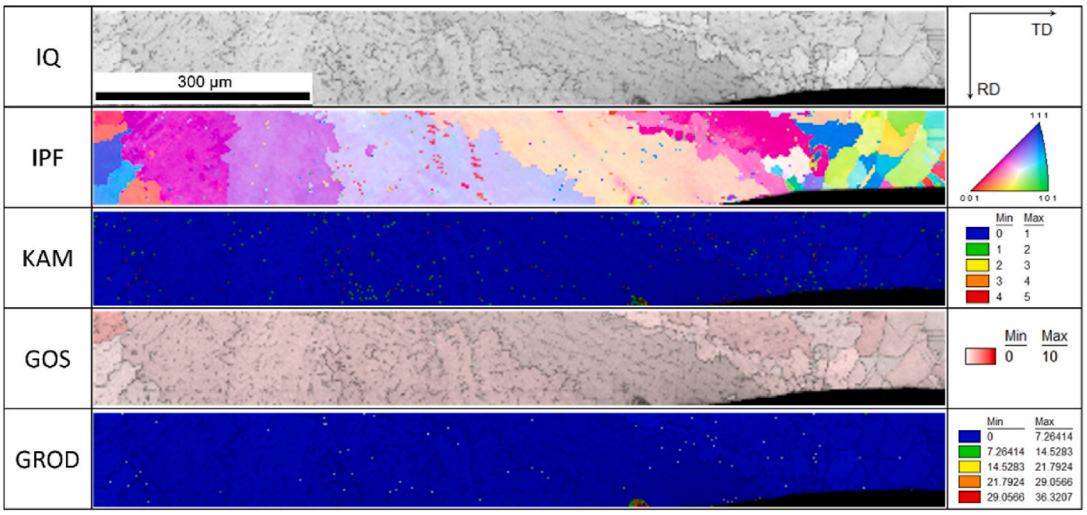

(a) Distance from the fusion line: $x = 0$ mm

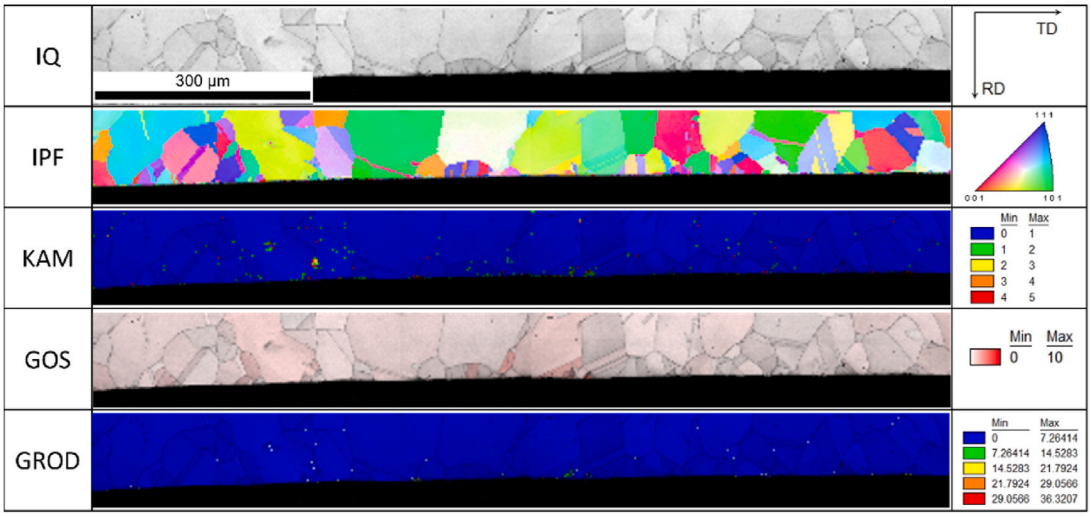

(b) Distance from the fusion line: $x = 1$ mm

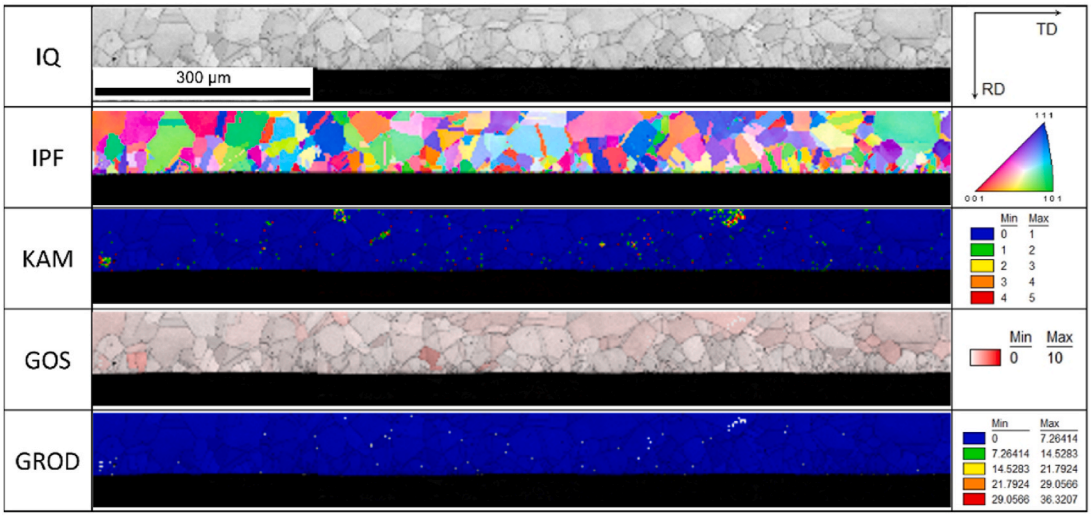

(c) Distance from the fusion line: $x = 2$ mm

Fig. 9. Crystal orientation maps near the fusion line of the 1-pass weld with surface machining.

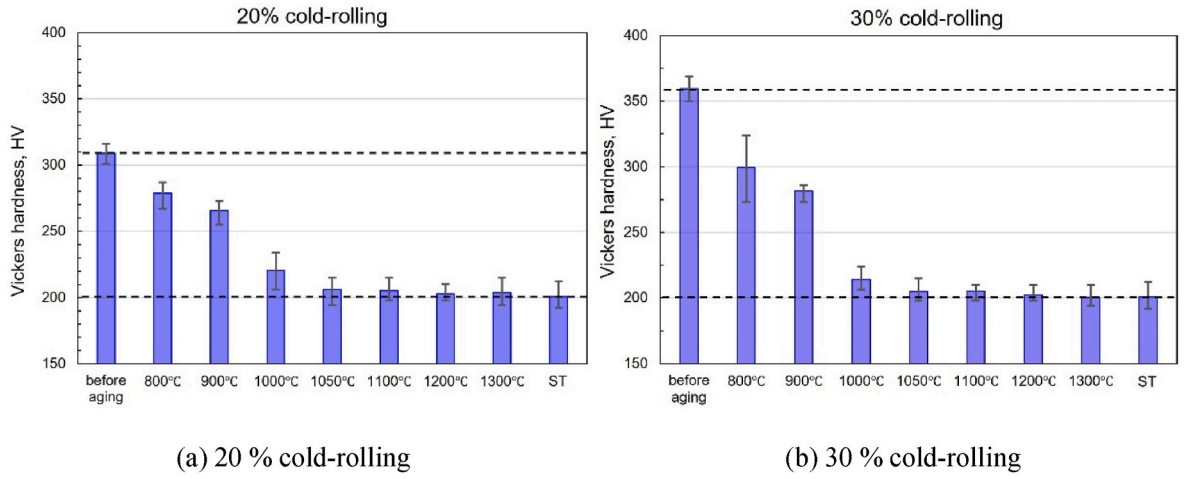

Fig. 10. Vickers hardness change behavior of cold-rolled specimens before and after thermal aging.

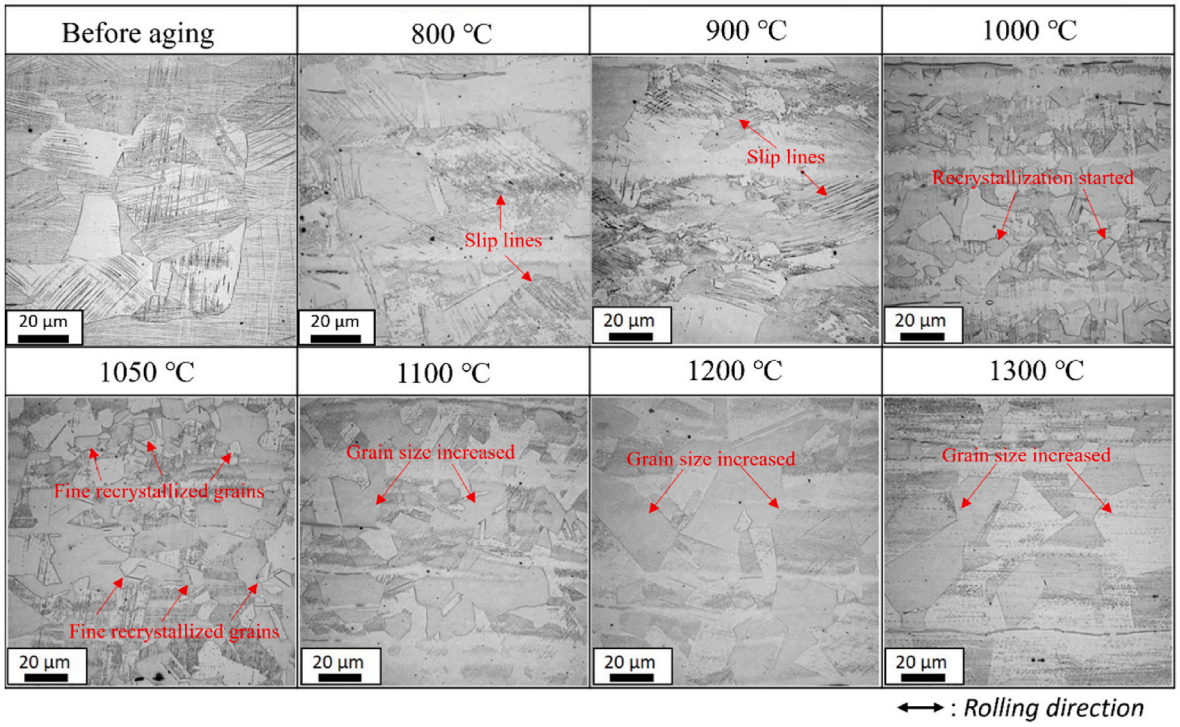

Fig. 11. Microstructures of 20 % cold-rolled specimens before and after heat treatment.

experimentally measured residual stress values in Ref. [27], the initial residual stress introduced by prior surface machining was set to a tensile residual stress of 400 MPa in the welding direction and 200 MPa in the direction perpendicular to the weld. The melting point of SUS316 austenitic stainless steel is 1400 °C, and its temperature-dependent material properties [20] are illustrated in Fig. 14.

Fig. 15 shows the simulated peak temperature distribution in the central cross section of 7-layer weld. The simulated WM part is shown in red color, where the peak temperature is over 1400 °C. The shape of the simulated WM is consistent with the actual WM shape, following that that the FEM simulated results were accurate.

Fig. 16 shows the simulation results of residual stress distribution in the welding direction (σ_y), direction perpendicular to the welding direction (σ_x), and plate thickness direction (σ_z) of the central cross section of 7-layer weld. Comparing the overall residual stress distribution, a large residual stress occurred in both the welding direction and the direction perpendicular to the welding direction after 7-layer welding. In the welding direction (y), significant residual stress occurred on the final pass side owing to the influence of final pass welding. A large tensile residual stress was confirmed to occur in the direction perpendicular to the welding direction (x), mainly near the bottom surface and fusion line. This is in good agreement with the locations where cracks occur during actual welding [28,29]. It was also found that there was almost no obvious stress in the plate thickness direction (z), even after 7-layer welding.

To verify the accuracy of the proposed annealing temperature of 1050 °C for SUS316 steel in FEM simulation, the actual residual stress was experimentally measured using a double exposure method (DEM).

For stress measurements of coarse-grained materials such as SUS316 steel, the strain scanning method using synchrotron radiation and the constant penetration depth method cannot obtain diffraction rings, making it difficult to measure with a 0-dimensional or 1-dimensional

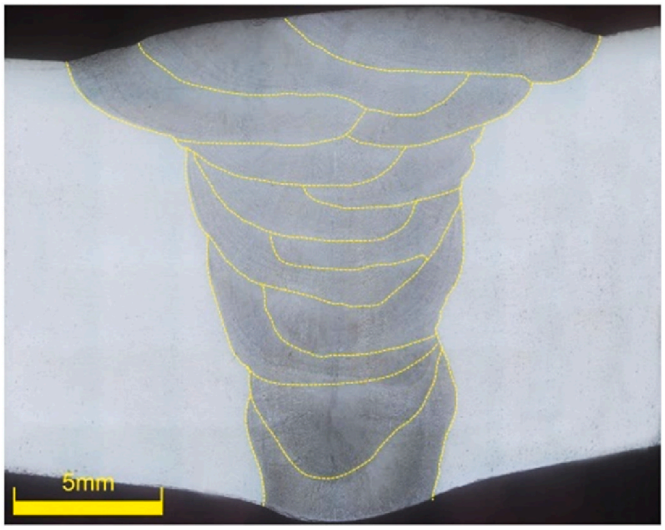

Fig. 12. Cross sectional view of 7-layer weld.

detector. To solve this problem, Suzuki et al. proposed a DEM using a 2-dimensional detector [24]. In addition, the detector can be applied to the X-ray stress measurement of coarse-grained materials by combining DEM with a CdTe pixel detector, which is capable of energy discrimination in the high-energy region [25]. There are many reports on the principle of stress measurement using the DEM [24,25]. When measuring the residual stress in welds using DEM, a complex diffraction pattern is obtained that contains a mixture of diffraction spots, continuous rings, and textures; therefore, a diffraction angle determination method using a cross-correlation algorithm is suitable [30], which was also used in this study.

Regarding the experimental results obtained by DEM as shown in Fig. 5, in the DEM system, the transmitted light was incident perpendicular to the specimen. Therefore, the experimentally measured strains are ε'_x and ε'_z,' respectively. In addition, if it is assumed that there is no stress in the thickness direction of the welded specimen and that it is in a plane stress state, the stress in the direction perpendicular to the welding direction (x) and the plate thickness direction (z) can be calculated using the following equations [31]: E and ν are the X-ray elastic constants of the 311 diffraction, Young's modulus, and Poisson's ratio, respectively.

$$\sigma_x = \frac{E}{(1+\nu)\cos^2\theta_0}\left[\varepsilon'_x + S'\left(\varepsilon'_z + \varepsilon'_x\right)\right] \quad (1)$$

$$\sigma_z = \frac{E}{(1+\nu)\cos^2\theta_0}\left[\varepsilon'_z + S'\left(\varepsilon'_z + \varepsilon'_x\right)\right] \quad (2)$$

$$S' = \frac{\nu}{(1+\nu)\cos^2\theta_0 - 2\nu} \quad (3)$$

According to the residual stress results measured by DEM, an actual residual stress map was created within 1 mm from the bottom surface of the 7-layer weld. Fig. 17 presents the residual stress map in the direction perpendicular to the welding direction (x). The coordinate position of the residual stress map is shown in Fig. 17 (a), where the horizontal axis $x = 0$ mm is the weld center line, the vertical axis $z = 0$ mm is the peak of the penetration bead, and the negative direction is the plate thickness direction. Fig. 17 (a) also shows schematic diagrams of the WM, HAZ, and BM. In the 7-layer welded specimen, a large tensile residual stress appeared in the HAZ ($x = \pm$ 5–10 mm) near the fusion line at the bottom of the weld. This indicates that the residual stress at the bottom of the weld was formed owing to the influence of final-pass welding. This

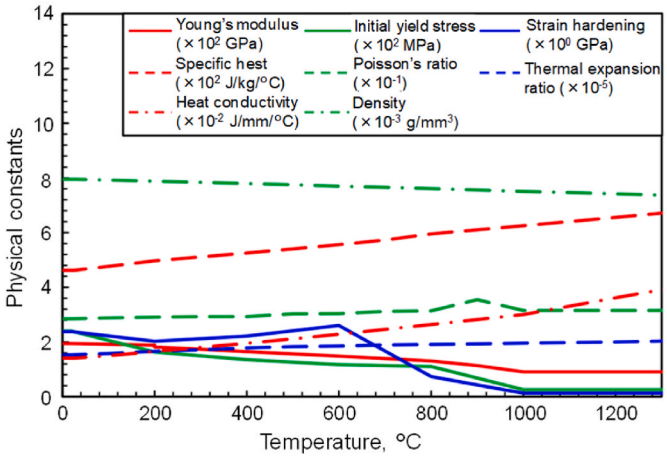

Fig. 14. Temperature-dependent material properties of SUS316 steel.

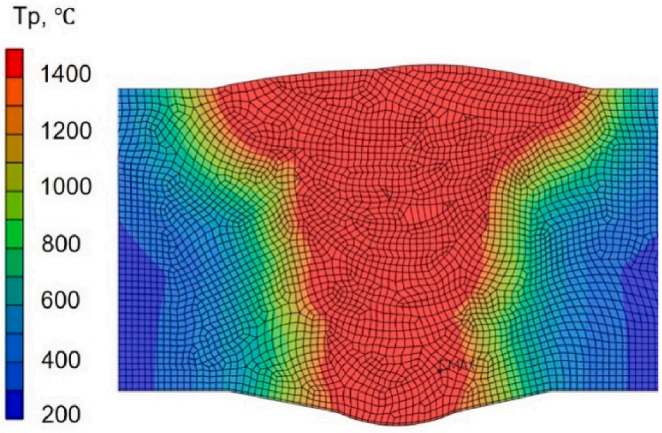

Fig. 15. Simulated peak temperature distribution at the cross section.

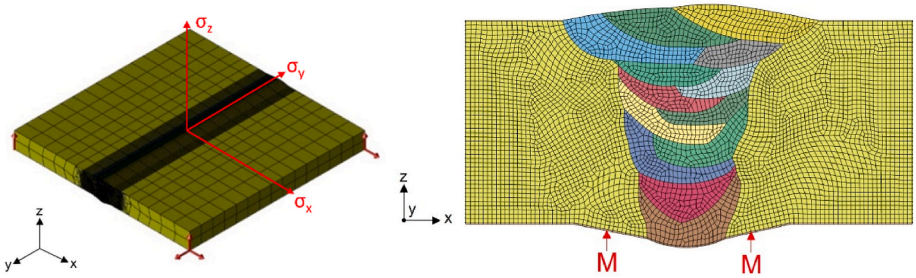

(a) Overall view (b) Sequence and arrangement of welds in the model

Fig. 13. FEM analysis model of 7-layer weld (M indicates the surface machining).

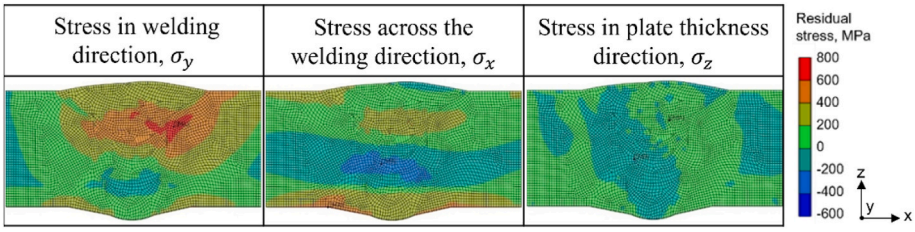

Fig. 16. Simulated residual stress distribution at the cross section in 3 directions.

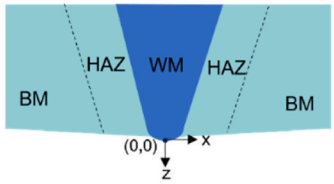

(a) Coordinate position

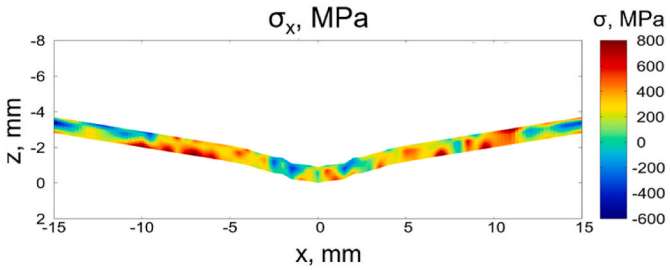

(b) Residual stress map

Fig. 17. Residual stress map near the surface in the direction perpendicular to the welding direction.

tensile residual stress distribution is consistent with the actual SCC cases in welds [28,29]. Furthermore, while there was no clear evidence of the effects of surface machining in the HAZ, there was a tensile residual stress of approximately 400 MPa in areas not heat affected by the welding thermal cycle (approximately $x = \pm 15$ mm), which is considered to be caused by the remaining surface machining effects.

Similarly, Fig. 18 shows the residual stress map in the plate thickness direction (z) of a 7-layer weld. It can be found that the residual stress in the direction of the plate thickness varied in the range of approximately −200~200 MPa, indicating that no significant residual stress was observed.

Fig. 19 illustrates the comparison between the FEM simulated and experimentally measured results of the residual stress distribution at $z = -0.6$ mm in the direction perpendicular to the welding direction of the 7-layer weld with surface machining. The FEM simulation results calculated using the proposed annealing temperature of 1050 °C for SUS316 are in good agreement with the experimentally measured results. It was confirmed in both cases that large tensile residual stress occurred in the HAZ ($x = \pm$ 5–10 mm) near the fusion line. Moreover,

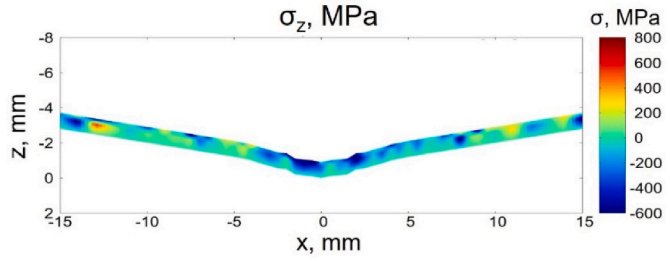

Fig. 18. Residual stress map near the surface in the plate thickness direction.

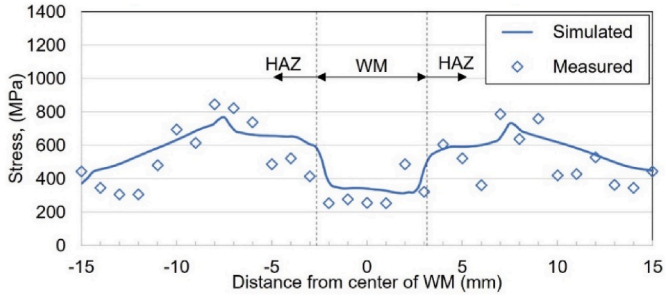

Fig. 19. Comparison between simulated residual stress and measured result in the direction perpendicular to the welding direction.

this tensile residual stress distribution is consistent with cases in which SCC occurs near the fusion line in actual welds [28,29]. Furthermore, no significant residual stress was observed in either the experimentally measured or FEM simulated results for the residual stress in the plate thickness direction.

In summary, using the proposed annealing temperature of 1050 °C, there is a good correspondence between the experimentally measured residual stress and the FEM simulated results. It follows the proposed annealing temperature of 1050 °C for SUS316 in FEM simulation is effective and reasonable. Therefore, the annealing temperature of 1050 °C should be included in the FEM simulation of SUS316 welding in the future. Thus, the appropriate welding conditions can be selected by high-precision FEM simulation before actual welding, which is very useful for the multilayer welding in the industry.

4. Conclusions

The recrystallization phenomenon of strain hardening during the welding process in SUS316 austenitic stainless steel was investigated in this study. In addition, a suitable annealing temperature in FEM simulation was proposed to simulate the phenomenon. The accuracy of the proposed annealing temperature was verified by comparing the simulated and measured residual stresses after multilayer welding. The following conclusions can be drawn.

(1) The EBSD analysis results of 1-pass welding with prior surface machining proved that the annealing effect can be introduced owing to the recrystallization phenomenon of strain hardening during the welding process. Therefore, it was necessary to introduce a suitable annealing temperature into the FEM simulation to simulate this phenomenon.

(2) To establish a propriate annealing temperature, the 20 % and 30 % pre-strained cold-rolled specimens were subjected to peak temperatures ranging from 800 °C to 1300 °C, held at the peak temperature for 1 s, and their corresponding hardness results showed that when the annealing temperature is approximately 1050 °C, the resulting hardness aligns with that of solution-treated specimens. Therefore, it was determined that the

appropriate annealing temperature in the FEM simulation of SUS316 steel is 1050 °C.

(3) To verify the accuracy of the proposed annealing temperature in the FEM simulation, the determined annealing temperature (1050 °C) was applied in the FEM model to estimate the residual stress after 7-layer welding, with the results validated through measurements. The good correspondence between the simulated residual stress and the measured results follows that the proposed annealing temperature of 1050 °C for SUS316 in FEM simulation is effective and reasonable. Therefore, the annealing temperature of 1050 °C should be included in the FEM simulation of SUS316 welding in the future. Thus, the appropriate welding conditions can be selected by high-precision FEM simulation before actual welding, which is very useful for the multilayer welding in the industry.

CRediT authorship contribution statement

Lina Yu: Writing – review & editing, Writing – original draft, Methodology, Formal analysis, Data curation, Conceptualization. **Kenji Suzuki:** Software, Methodology, Data curation. **Hiroyuki Hirata:** Supervision, Conceptualization. **Kazutoshi Nishimoto:** Supervision, Conceptualization. **Kazuyoshi Saida:** Supervision, Conceptualization.

Declaration of competing interest

The authors declared that they have no conflicts of interest to this work.

We declare that we do not have any commercial or associative interest that represents a conflict of interest in connection with the work submitted.

Acknowledgment

FundingThis research was funded by Kansai Electric Power Co., Inc., Japan.

The authors gratefully acknowledge the support for the synchrotron radiation experiments provided by the SPring-8 Research Project (No. 2023B1991). The authors gratefully acknowledge Prof. Ninshu Ma of Osaka University for the assistance with FEM simulation.

Data availability

Data will be made available on request.

References

[1] K. Sieradzki, R.C. Newman, Stress-corrosion cracking, J. Phys. Chem. Solid. 48 (1987) 1101–1113, https://doi.org/10.1016/0022-3697(87)90120-X.

[2] X. Xie, D. Ning, B. Chen, S. Lu, J. Sun, Stress corrosion cracking behavior of cold-drawn 316 austenitic stainless steels in simulated PWR environment, Corros. Sci. 112 (2016) 576–584, https://doi.org/10.1016/j.corsci.2016.08.014.

[3] M. Aoki, T. Terachi, T. Yamada, K. Arioka, A study on SCC behavior in weld heat-affected zone of stainless steels – influences of distance from a weld line, INSS J 19 (2012) 118–130. https://www.inss.co.jp/wp-content/uploads/2017/03/2012_19J118_130.pdf.

[4] L. Yu, K. Nishimoto, K. Saida, Effect of dynamic strain aging on hardness in the heat-affected zone of SUS316 steel welds, J. Mater. Sci. Eng. A. 13 (2023) 13–25. https://www.davidpublisher.com/Public/uploads/Contribute/64642275e39e4.pdf.

[5] L. Yu, K. Nishimoto, H. Hirata, K. Saida, Hardness prediction of the heat-affected zone in multilayer welded SUS316 stainless steel based on dislocation density change behavior, Metall. Mater. Trans. A. 55 (2024) 1788–1803, https://doi.org/10.1007/s11661-024-07318-7.

[6] D. Deng, S. Kiyoshima, Influence of annealing temperature on calculation accuracy of welding residual stress in a SUS304 stainless steel joint, Acta Metall. Sin. 50 (2014) 626–632. https://www.ams.org.cn/CN/10.3724/SP.J.1037.2013.00565.

[7] D. Deng, H. Murakawa, Prediction of welding residual stress in multi-pass butt-welded modified 9Cr-1Mo steel pipe considering phase transformation effects, Comput. Mater. Sci. 37 (2006) 209–219, https://doi.org/10.1016/j.commatsci.2005.06.010.

[8] D. Deng, H. Murakawa, Numerical simulation of temperature field and residual stress in multi-pass welds in stainless steel pipe and comparison with experimental measurements, Comput. Mater. Sci. 37 (2006) 269–277, https://doi.org/10.1016/j.commatsci.2005.07.007.

[9] D. Deng, H. Murakawa, W. Liang, Numerical and experimental investigations on welding residual stress in multi-pass butt-welded austenitic stainless steel pipe, Comput. Mater. Sci. 42 (2008) 234–244, https://doi.org/10.1016/j.commatsci.2007.07.009.

[10] Y. Javadi, M. Akhlaghi, M.A. Najafabadi, Using finite element and ultrasonic method to evaluate welding longitudinal residual stress through the thickness in austenitic stainless steel plates, Mater. Des. 45 (2013) 628–642, https://doi.org/10.1016/j.matdes.2012.09.038.

[11] Y. Ueda, K. Nakacho, T. Shimizu, Improvement of residual stresses of circumferential joint of pipe by heat-sink welding, J. Press, Vessel Technol. 108 (1986) 14–23, https://doi.org/10.1115/1.3264746.

[12] W.L. Zang, J. Gunnars, P.S. Dong, J.K. Hong, Improvement and validation of weld residual stress modelling procedure, Swedish Radiation Safety Authority 15 (2009) (2009) 1–42. https://inis.iaea.org/collection/NCLCollectionStore/_Public/40/086/40086697.pdf.

[13] J.J. Xu, P. Gilles, Y.G. Duan, C. Yu, Temperature and residual stress simulations of the NeT single-bead-on-plate specimen using SYSWELD, Int. J. Pres. Ves. Pip. (2012) 99–100, https://doi.org/10.1016/j.ijpvp.2012.08.002, 51–60.

[14] O. Muránsky, C.J. Hamelin, M.C. Smith, P.J. Bendeich, L. Edwards, The effect of plasticity theory on predicted residual stress fields in numerical weld analyses, Comput. Mater. Sci. 54 (2012) 125–134, https://doi.org/10.1016/j.commatsci.2011.10.026.

[15] O. Muránsky, C.J. Hamelin, V.I. Patel, V. Luzin, C. Braham, The influence of constitutive material models on accumulated plastic strain in finite element weld analyses, Int. J. Solid Struct. 69–70 (2015) 518–530, https://doi.org/10.1016/j.ijsolstr.2015.04.032.

[16] Q. Wang, X.S. Liu, P. Wang, X. Xiong, H.Y. Fang, Numerical simulation of residual stress in 10Ni5CrMoV steel weldments, J. Mater. Process. Technol. 240 (2017) 77–86, https://doi.org/10.1016/j.jmatprotec.2016.09.011.

[17] X. Yu, D. Qiao, Z. Feng, P. Crooker, Y. Wang, High temperature dynamics strain hardening behavior in stainless steels and nickel alloys, in: Proceedings of the ASME 2014 Pressure Vessels and Piping Conference, ASME, Anaheim, California, 2014, https://doi.org/10.1115/PVP2014-28869. V06BT06A072.

[18] L. Geng, S. Tu, J. Gong, W. Zhang, Simulation of residual stress in butt girth welding of ultra-thick 13MnNiMoR steel cylinder by different material hardening models, Mater. Mech. Eng. 43 (2019) 60–66, https://doi.org/10.11973/jxgccl201903012.

[19] X. Yu, P. Crooker, Y. Wang, Z. Feng, High-temperature deformation constitutive law for dissimilar weld residual stress modeling: effect of thermal load on strain hardening, in: Proceedings of the ASME 2015 Pressure Vessels and Piping Conference, ASME, Boston, Massachusetts, 2015 V06BT06A073, https://doi.org/10.1115/PVP2015-45776.

[20] D. Deng, S. Kiyoshima, Numerical simulation of residual stresses induced by laser beam welding in a SUS316 stainless steel pipe with considering initial residual stress influences, Nucl. Eng. Des. 240 (2010) 688–696, https://doi.org/10.1016/j.nucengdes.2009.11.049.

[21] D. Deng, S. Kiyoshima, FEM analysis of residual stress distribution near weld start/end location in thick plates, Comput. Mater. Sci. 50 (2011) 2459–2469, https://doi.org/10.1016/j.commatsci.2011.03.027.

[22] R. Ihara, S. Okano, M. Mochizuki, Numerical analysis of residual stress distribution generated by welding after surface machining based on hardness variation in surface machined layer due to welding thermal cycle, Weld. Int. 31 (2017) 111–121, https://doi.org/10.1080/09507116.2016.1223202.

[23] S. Li, W. Chen, L. Hu, D. Deng, Influence of strain hardening and annealing effect on the prediction of welding residual stresses in a thick-wall 316 stainless steel butt-welded pipe joint, Acta Metall. Sin. 57 (2021) 1653–1666. https://www.ams.org.cn/EN/10.11900/0412.1961.2020.00534.

[24] K. Suzuki, T. Shobu, A. Shiro, Stress measurement of coarse grains using double exposure method, J. Soc. Mater. Sci. Jpn. 68 (2019) 312–317, https://doi.org/10.2472/jsms.68.312.

[25] K. Suzuki, M. Yamada, A. Shiro, T. Shobu, H. Toyokawa, C. Saji, Stress measurements of quasi-coarse grained material using double exposure method with high-energy monochromatic X-rays, J. Soc. Mater. Sci. Jpn. 71 (2022) 347–353, https://doi.org/10.2472/jsms.71.347.

[26] D. Deng, H. Murakawa, M. Shibahara, Investigations on welding distortion in an asymmetrical curved block by means of numerical simulation technology and experimental method, Comput. Mater. Sci. 48 (2010) 187–194, https://doi.org/10.1016/j.commatsci.2009.12.027.

[27] R. Ihara, M. Mochizuki, Effect of processing conditions on residual stress distributions by bead-on-plate welding after surface machining, J. Soc. Mater. Sci. Jpn. 63 (2014) 551–556, https://doi.org/10.2472/jsms.63.551.

[28] Y. Okamura, H. Yamashita, T. Fukuda, T. Futami, Structural integrity evaluation for core shroud and PLR piping with SCC, Pressure engineering 43 (2005) 4–14. https://www.jstage.jst.go.jp/article/hpi/43/1/43_1_4/_article.

[29] Y. Okamura, A. Sakashita, T. Fukuda, H. Yamashita, T. Futami, Latest SCC issues of core shroud and recirculation piping in Japanese BWRs, in: Transactions of the 17th International Conference on Structural Mechanics in Reactor Technology,

2003. https://repository.lib.ncsu.edu/server/api/core/bitstreams/316a7903-3e28-4713-9610-82d4aecd45d6/content.

[30] K. Suzuki, Y. Miura, Diffraction angle determination using cross-correlation algorithm for double exposure method, J. Soc. Mat. Sci. Japan. 73 (2024) 286–292, https://doi.org/10.2472/jsms.73.286.

[31] K. Suzuki, K. Kura, Y. Miura, A. Shiro, H. Toyokawa, C. Saji, K. Kajiwara, T. Shobu, A study on stress measurement of weld part using double exposure method, J. Soc. Mater. Sci. Jpn. 71 (2022) 1005–1012, https://doi.org/10.2472/jsms.71.1005.